HIMU geochemical signature originating from the transition zone

Shichun Huang [a,*], Oliver Tschauner [a,*], Shuying Yang [b], Munir Humayun [b], Wenjun Liu [c], Stephanie N. Gilbert Corder [d], Hans A. Bechtel [d], Jon Tischler [c]

[a] *Department of Geoscience, University of Nevada Las Vegas, Las Vegas, NV 89154, USA*
[b] *National High Magnetic Field Laboratory and Department of Earth, Ocean & Atmospheric Science, Florida State University, Tallahassee, FL 32310, USA*
[c] *Advanced Photon Source, Argonne National Laboratory, Lemont, IL 60439, USA*
[d] *Advanced Light Source, Lawrence Berkeley National Laboratory, Berkeley, CA 94720, USA*

ARTICLE INFO

ABSTRACT

Plume volcanism may sample mantle sources deeper than mid-ocean ridge and arc volcanism. Ocean island basalts (OIBs) are commonly related to plume volcanism, and their diverse isotopic and elemental compositions can be described using a limited number of mantle endmembers. However, the origins and depths of these mantle endmembers are highly debated. Here we show that the HIMU (high μ, $\mu = {}^{238}U/{}^{204}Pb$) endmember may reside in the transition zone. Specifically, we report the geochemical signature of a high-pressure multiphase diamond inclusion, entrapped at 420–440 km depth and 1450 $\pm$ 50 K, which matches exactly the geochemical patterns of the HIMU-rich OIBs. Since the HIMU component is variably sampled by almost all OIBs, our finding implies that the transition zone causes a major overprint of the geochemical features of mantle plumes. Some mantle plumes, like those feeding Bermuda, St Helena, Tubuai and Mangaia, appear to be dominated by this source. Furthermore, our finding highlights the importance of the transition zone in highly incompatible element budget of the mantle.

1. Introduction

The geochemical and isotopic features of ocean island basalts (OIBs) are different from those of mid-ocean ridge basalts (MORBs) and island arc basalts (IABs) (White et al., 2015), and they are thought to be produced by mantle plumes that may rise from the deep mantle or at least markedly greater depth than the MORB extraction regions (e.g., White et al., 2015; Montelli et al., 2004; Humayun et al., 2004; Huang et al., 2011; Weis et al., 2011; Trela et al., 2017; Rizo et al., 2019; Williams et al., 2019). The diverse isotopic and elemental compositions of OIBs require a heterogeneous mantle, and only several mantle endmembers, such as EM-I, EM-II (enriched mantle), HIMU (high μ, $\mu = {}^{238}U/{}^{204}Pb$), DMM (depleted MORB mantle), and FOZO (FOcus ZOne, high ${}^3He/{}^4He$), are needed to explain the observed isotopic variations (e.g., White et al., 2015; Jackson and Dasgupta, 2008; Huang et al., 2017). While the isotopic and elemental compositions of mantle endmembers are well-constrained by the analysis of erupted lavas (White et al., 2015), their locations in the mantle are poorly understood. Cor-

relations between OIB isotopic signatures observed at the Earth's surface and seismic structures in the mantle suggest that some mantle endmembers may be located in the deep mantle (e.g., Hart, 1984; Huang et al., 2011; Weis et al., 2011; Chauvel et al., 2012; Williams et al., 2019). Some geochemical and isotopic signatures in OIBs, such as high Fe/Mn (Humayun et al., 2004), high ${}^{186}Os/{}^{188}Os$ (Brandon and Walker, 2005), and low ${}^{182}W/{}^{184}W$ (Rizo et al., 2019), have been used to infer an origin at the core-mantle boundary. More recently, some geochemical signatures, such as high K/U in EM-1 type Cenozoic potassic basalts from Northeastern China (Wang et al., 2017) and high U/Pb in SiO_2-undersaturated HIMU lavas from Bermuda (Mazza et al., 2019), are attributed to the presence of residual liebermannite (Grassi et al., 2012), a high-pressure polymorph of K-feldspar previously labeled as K-hollandite (Ringwood et al., 1967; Ma et al., 2018), in their mantle sources. Liebermannite is stable between 14 and 20 GPa in basaltic rocks (Litasov and Ohtani, 2005). If present, mantle plumes that contribute to those basalts (Wang et al., 2017; Mazza et al., 2019) have to originate from the transition zone. Here, we report that the elemental features of HIMU-rich OIBs, such as Bermuda, St Helena, and Cook-Austral, exactly match the geochemical signature of a multiphase inclusion of transition zone phases in a diamond. We show that HIMU represents an enriched layer or array of regions in the transition zone that is linked to subducted MORB.

* Corresponding authors.
E-mail addresses: shichun.huang@unlv.edu (S. Huang), olivert@physics.unlv.edu (O. Tschauner).
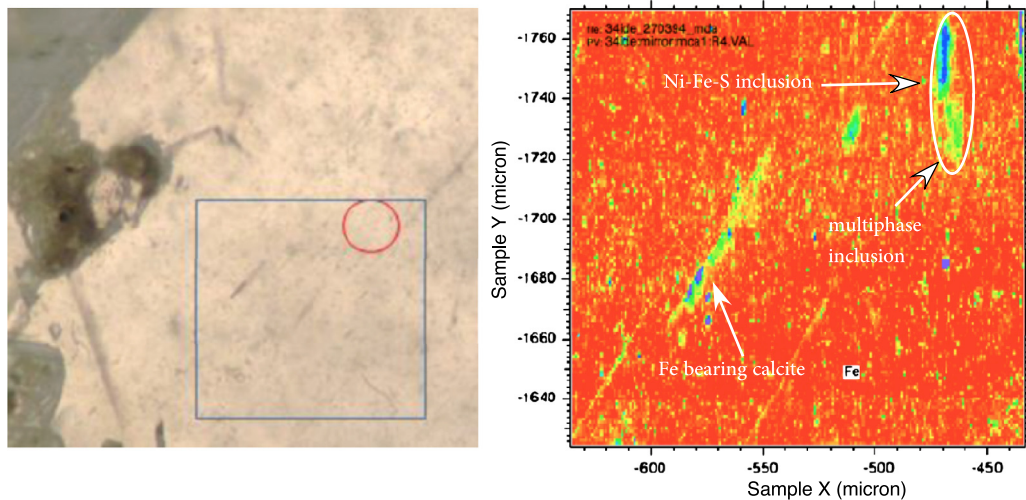
Fig. 1. a. Diamond ONZiZ-74. Red circle: area of inclusion. Blue rectangle: Area of XRF (X-ray fluorescence) map (tilted by ∼10°). Each side of the rectangle is 200 μm. **b.** X-ray fluorescence map of Fe with a 2 μm × 2 μm grid. The elongated inclusion between −1765 and −1720 (Height) and X = −460 to −470 is the garnet-10Å phase-liebermannite-ilmenite inclusion. Ilmenite is between X = −460 to −465 and Height = −1720 to −1740. (For interpretation of the colors in the figure(s), the reader is referred to the web version of this article.)

2. Sample studied and analytical techniques

The studied single crystal diamond specimen was a 1.0 mm thick and triangular-shaped piece, with top and bottom faces normal to [111], which was obtained through cleaving and subsequent polishing of a so-called 'coated' octahedral diamond. The coating is a natural late-stage overgrowth of diamond on an existing diamond crystal, which is not visible in Fig. 1a and not further studied here. The specimen belongs to the Caltech mineral collection with specimen number ON-ZiZ74a and is of unknown provenance. The diamond inclusion was identified through synchrotron micro-X ray fluorescence (XRF) and diffraction (XRD) mapping. Subsequently, in-situ Laser Ablation Inductively Coupled Plasma Mass Spectrometry (LA-ICP-MS) was used for chemical analysis.

XRF and XRD data were collected at the undulator beamline 34-IDE at the Advanced Photon Source, Argonne National Laboratory. The primary X-ray beam had an energy of 24.000 keV. The beam was focused by elliptical mirrors to 0.4×0.6 μm^2 laterally. Grid size was set to 4×4 μm^2 for XRF mapping, and 2×2 μm^2 for diffraction mapping.

The specimen was mounted on a motorized x-y-z stage with sub- μm motion precision and centered in the beam waist of the focused X-ray beam based on a high-magnification optical system that was aligned previously with an X-ray fluorescent YAG crystal. The X-ray focal spot beam waist is ∼300 μm in depth and samples almost the entire thickness of the sample without significant loss of X-ray flux density. Diffraction data were collected in mapping mode over a 40×40 μm^2 grid in 2 μm steps with 10 s acquisition time per frame. Frames from adjacent diamond matrix were used for diffraction frame background subtraction.

X-ray emission spectra were recorded with a Vortex Si drift detector for the Kα or −α$_1$ lines, respectively, of Ca, Ti, Cr, Fe, Ni, and Cu. Diffraction data were recorded with a MAR165 CCD area detector, calibrated and corrected for geometric distortion with Dioptas (Prescher and Prakapenka, 2015). Powder-like diffraction data were subsequently integrated with Dioptas and examined for phase identification, phase quantification, unit cell parameters, and site fractional occupancies with the Rietveld refinement method using the Powdercell algorithm (Kraus and Nolze, 1996).

Crystallites of spatial dimensions of the primary beam (0.4×0.6 μm^2) gave single-crystal diffraction patterns and were analyzed with the GSE-ADA and RSV software packages (Dera et al., 2013) for indexation and unit cell refinement. Subsequently, the |F(hkl)| of the observed reflections were used to assess site fractional occupancies (SFO) with the Endeavour reversed Monte Carlo algorithm for local optimization (Putz et al., 1999). No charges and no potentials were used in the optimization. We assessed SFOs through equivalent relative electron densities at occupied Wyckoff sites, following the method presented in Ma et al. (2019).

Infrared (IR) spectra were collected in transmission at beamline 1.4 at the Advanced Light Source, Lawrence Berkeley National Laboratory, with a Nicolet Magna 760 FTIR bench and a Nic-Plan IR microscope with a 32x magnification Schwarzschild objective, with 1 cm^{-1} resolution and a HgCdTe detector with a KBr beam splitter. Apertures were set to 40×60 μm^2 spatial resolution. Maps were collected over the same area as in the XRF map. A synthetic type II diamond was used for assessing the absorbance between 1000 and 1500 cm^{-1}.

Elemental abundances of the diamond inclusion were measured using LA-ICP-MS technique, on a Thermo Element XR™ ICP-MS coupled with an ElectroScientific Instruments (ESI) New Wave™ UP193FX excimer (193 nm) laser ablation system at the Plasma Analytical Facility of the National High Magnetic Field Laboratory, Florida State University. The laser ablation system was operated using spot mode, with a spot size of 150 μm, 50 Hz repetition rate, and 80% energy output corresponding to 12.6 J·cm^{-2}. In order to resolve the complicated carbon-related molecular interferences on low mass isotopes, all peaks were collected in medium mass resolution (m/Δm = 4,000). To compensate for the diminished signals, Jet Sampler and X-skimmer cones were used. Peaks of ^{7}Li, ^{9}Be, ^{12}C, ^{13}C, ^{16}O, ^{23}Na, ^{24}Mg, ^{27}Al, ^{28}Si, ^{31}P, ^{32}S, ^{39}K, ^{44}Ca, ^{45}Sc, ^{47}Ti, ^{51}V, ^{52}Cr, ^{55}Mn, ^{56}Fe, ^{59}Co, ^{60}Ni, ^{63}Cu, ^{66}Zn, ^{69}Ga, ^{74}Ge, ^{85}Rb, ^{88}Sr, ^{89}Y, ^{90}Zr, ^{93}Nb, ^{133}Cs, ^{138}Ba, ^{139}La, ^{140}Ce, ^{141}Pr, ^{145}Nd, ^{147}Sm, ^{153}Eu, ^{159}Tb, ^{160}Gd, ^{164}Dy, ^{165}Ho, ^{166}Er, ^{169}Tm, ^{174}Yb, ^{175}Lu, ^{180}Hf, ^{181}Ta, ^{208}Pb, ^{232}Th, and ^{238}U were monitored using magnet peak jumping technique and the Element's EScan mode by varying the acceleration voltage. The mass window was 10%, and the acquisition time was 0.1 second per peak. ^{40}Ar^{40}Ar peak was used as the lock mass. Blanks were measured on a piece of broken diamond anvil provided by Dr. A. Salamat. The raw count rates were processed manually. Measured count ratios referenced to ^{28}Si were converted to elemental abundance ratios referenced to Si using glass standard GSE-1G (Jochum et al., 2005). The elemental compositions were then calculated assuming that the sum of all the major oxides is 100% (Yang et al., 2015), and are reported in Table 1. Note that the reported compositions are volatile-free, because volatiles such

Table 1
Composition of diamond inclusion 11-ON-ZIZ.

		11-ON-ZIZ	Detection limit
Na$_2$O	%	2.80	0.08
MgO	%	5.4	0.1
Al$_2$O$_3$	%	9.5	0.2
SiO$_2$	%	40	
P$_2$O$_5$	ppm	17409	1328
K$_2$O	%	6	2
CaO	%	21.8	0.7
Sc	ppm	23	1
TiO$_2$	%	1.80	0.05
V	ppm	131	23
Cr	ppm	1111	79
MnO	%	0.12	0.02
FeOT	%	12.6	0.1
Co	ppm	80	45
Ni	ppm	2075	797
Cu	ppm	6020	74
Zn	ppm	6506	138
Ga	ppm	83	14
Rb	ppm	181	87
Sr	ppm	4389	92
Y	ppm	165	38
Zr	ppm	967	89
Nb	ppm	413	33
Cs	ppm	10	27
Ba	ppm	6658	72
La	ppm	990	31
Ce	ppm	2067	13
Pr	ppm	203	35
Nd	ppm	813	236
Sm	ppm	116	150
Eu	ppm	32	14
Tb	ppm	13	32
Gd	ppm	107	30
Dy	ppm	63	88
Ho	ppm	15	39
Er	ppm	49	30
Tm	ppm	3	35
Yb	ppm	26	36
Lu	ppm	0.6	33
Hf	ppm	0	159
Ta	ppm	21	35
Pb	ppm	858	21
Th	ppm	80	34
U	ppm	9	23

Detection limit is defined as 3 standard deviations above the background.

as CO$_2$ and H$_2$O could not be measured using our technique. The detection limits were estimated using three times the standard deviation of blank measurements.

3. Results

3.1. Synchrotron XRF elemental mapping and XRD patterns

Fig. 1 shows the visible light image and the corresponding map of the Fe Kα_1 emission line. Various impurities and inclusions are visible: The outcrop of two parallel cracks in the diamond is noticeable both in the visible light image (Fig. 1a) and through chemical impurities in the XRF map (Fig. 1b). Another Fe-rich area in the bottom of the map above these two cracks and with similar strike is from the siderite-component of calcite that has penetrated along a crack into the diamond crystal. Its intersection with the surface is barely visible in Fig. 1a. The entrapment pressure of this calcite is about ambient based on XRD measurement, and it is not further discussed in this study. One inclusion of very different orientation than those mentioned above was found to be from a silicate- and oxide inclusion with remnant pressure of 5-7 GPa (see below). As we will show, this high remnant pressure indicates entrapment in the deeper mantle and this inclusion was analyzed by LA-ICP-MS. The studied multi-phase inclusion is not intersect-

ing the surface, and its location is indicated through the red circle in Fig. 1a. In the XRF map, it covers the region between −1765 and −1720 μm (Height) and X = −460 to −470 μm. A representative diffraction image taken from the center of the inclusion is shown in Fig. 2. Single crystal-like reflections in this image belong to garnet. Weaker Debye-fringes from fine-grained material are from the sodic 10Å phase (TAP) (Howe and Pawley, 2019), ilmenite, and a minor amount of liebermannite. At the left border of the inclusion is an Fe-Ni-Cu-sulfide grain which is well separated from the silicate-oxide inclusion in the XRD maps but was ablated by LA-ICP-MS along with the silicate- and oxide phases.

The compositions of individual phases in the silicate inclusion were assessed based on phase proportions (Fig. 2), site occupancies, and bulk composition (Table 1), and are presented in Table 2. The phases are majorite-rich garnet, ilmenite, sodic TAP, and liebermannite. TAP occurs as fine-grained material of 20-30 nm average grain size (based on the Scherrer equation), and generates powder-like diffraction (Fig. 2a). This diffraction signal was analyzed by Rietveld refinement (Fig. 2b).

Ilmenite occurs as fine-grained material, and gives powder-like diffraction. The integrated diffraction pattern and the Rietveld-refined model pattern are shown in Fig. 2c. The refined unit cell volume was used for assessing a remnant pressure of 7 to 10 GPa for ilmenite of 3 to 8 mol% geikielite component based on the equations of state by Tronche et al. (2010), Yamanaka et al. (2007), and Wechsler and Prewitt (1984). Correction for elastic relaxation of surrounding diamond (Angel et al., 2014) would shift the lower and upper bound by 1-2 GPa. However, ilmenite is part of an aggregate of four phases, and elastic relaxation is probably much smaller. Liebermannite amounts to less than 7 % of the aggregate based on modal composition, and cannot be clearly identified through XRD. Some weak features in the diffraction pattern can be assigned to liebermannite (Fig. 2c) at a remnant pressure of 6 ± 1 GPa, based on its equation of state (Ballaran et al., 2009).

The garnet generates single crystal diffraction and was indexed as tetragonal (Fig. 2a). Ca-rich majoritic garnet assumes commonly a tetragonal rather than cubic metric (Hazen et al., 1994). Garnet composition was assessed through a) refinement of site occupancies, b) bulk elemental abundances of the diamond inclusion (Table 1), and c) the phase proportions of ilmenite, TAP and liebermannite as constraints on the remaining element budget. Rietveld refinement based on the powder-like diffraction of ilmenite and TAP gives the proportions of these two phases and site occupancies, and liebermannite was originally not considered. With these constraints on compositions and the relative amounts of ilmenite and TAP, a garnet composition was assessed to match the site occupancies obtained from XRD data. We note that refinement of site occupancies assesses relative electron density rather than chemical species. This relative electron density was used as constraint to assign site occupancies for elements as described above. Residual elemental abundance matches the composition of liebermannite (Table 2). Allowing for the maximal amount of K in garnet, the dominant phase in the aggregate, the amount of liebermannite would be reduced by ∼ 30%. However, this implies an amount of excess silica that is beyond the uncertainties of the analysis of garnet and the TAP phase. No free phase of silica (stishovite) has been detected in the diffraction patterns but an upper bound of stishovite can be assessed in the Rietveld refinement to < 1.7 vol%. This places a lower bound of 5 mol% on the abundance of liebermannite. Liebermannite in paragenesis with garnet of similar composition as observed here has also been reported in a recent experimental study (Greaux et al., 2018) although not in paragenesis with the TAP phase. The garnet composition and structure are given in Tables 3 and S1.

Rietveld refinement of ilmenite, sodic TAP, and liebermannite converged to a wRp of 0.11 and an Rp of 0.08, with profile terms
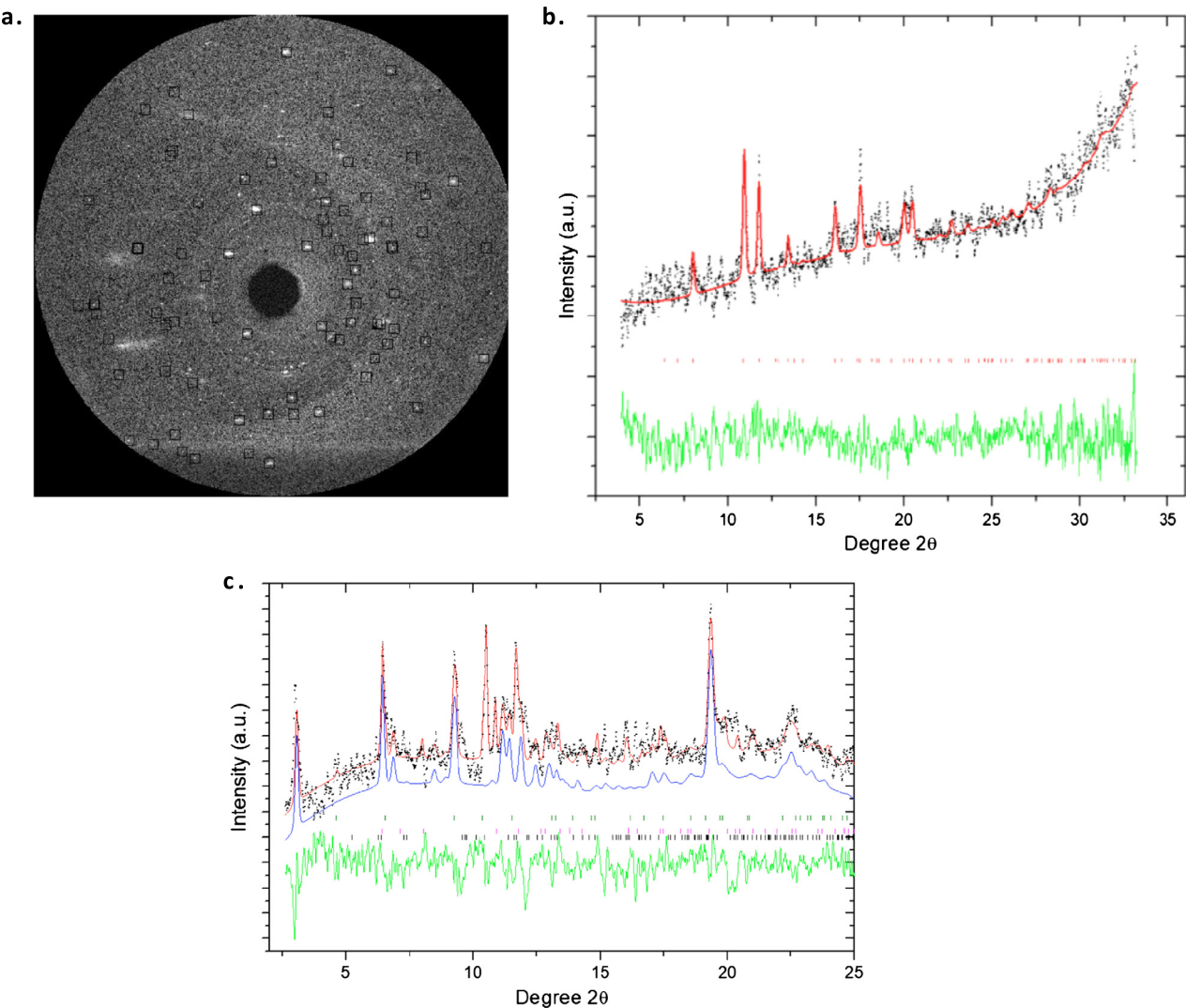
a.

b.

c.

Fig. 2. a. Diffraction frame taken from the center of the inclusion. Garnet generates single crystal diffraction. The peaks (black boxes) were fitted and integrated and used for indexation and structure refinement. TAP, minor ilmenite, and possibly liebermannite generate the faint Debye fringes superimposed on the garnet single crystal pattern. **b.** Integrated diffraction pattern of ilmenite (black crosses), red: Rietveld-refined calculated pattern of ilmenite, green: residual of fit, tick marks indicate Bragg angles of allowed reflections. The refined unit cell of ilmenite is $a = b = 5.04(1)$, and $c = 13.77(10)$ Å. **c.** Integrated diffraction pattern of fine-grained fraction from panel a (black crosses). The Rietveld-refined pattern of TAP, ilmenite, liebermannite, and garnet is shown in red. The fully |F(hkl)|-weighted portion of TAP is shown in blue with offset. Garnet single crystal reflections were masked but some minor reflections of smaller crystallites remain and were fitted with the LeBail approach. Green: residual of fit. Tickmarks: dark green = liebermannite, black = garnet, magenta = ilmenite. The unit cell dimensions of the sodic TAP are $5.344(6) \times 9.22(4) \times 9.64(6)$ Å^3, $\beta = 95.5(6)°$. Crystallographic information files will be deposited with the ICSD (Inorganic Crystal Structure Database).

Table 2

Molar fractions and compositions of the minerals in the inclusion. Eskolaite is probably in solid solution with ilmenite and was not detected as free phase. The X_{maj} in garnet is between 0.54 and 0.71 (Collerson et al., 2010) that corresponds (with uncertainties) to a formation pressure of 14–20 GPa. Based on Wijbrans et al. (2014), one obtains a pressure of formation between 9 and 36 GPa. Stishovite was not observed as free phase and would be less than 2%.

	Garnet	TAP	Liebermn	Ilmenite	Eskolaite
Na$_2$O	0.24(2)	0.14(1)	0.06(6)	0	0
MgO	0.35(1)	2.63(1)	0	0.08(5)	0
Al$_2$O$_3$	0.53(2)	0.21(1)	1	0	0
SiO2	3.33(1)	3.79(1)	3	0	0
K$_2$O	0.4(4)	0.06(3)	0.95(5)	0	0
CaO	2.35(0)	0	0	0	0
Sc	0	0	0	0	0
TiO$_2$	0.13(6)	0	0	1	0.01(1)
V	0	0	0	0	0
Cr	0.06(6)	0	0	0	1.1(1.0)
MnO	0.01	0	0	0	0
FeOT	1.0(0)	0.19(2)	0	0.92(5)	0.10(7)
mol%	77.8(2.0)	10.8(1.2)	6.5(2)	2.9(9)	1(1)

Table 3

Atomic coordinates and isotropic displacement parameters (in Å^2) of the garnet. The garnet is tetragonal with cell dimension of $a = 11.23(4)$ and $c = 11.67(7)$ Å, which gives a volume of 1471(8) Å^3.

| Atom	Wyck.	Occ.	x	y	z	U
CaX1	8b	0.69(1)	0	0	1/4	0.0038(4)
MgX1	8b	0.20(1)	0	0	1/4	0.0038(4)
NaX1	8b	0.10(2)	0	0	1/4	0.0038(4)
FeX1	8b	0.01(1)	0	0	1/4	0.0038(4)
CaX2	16e	0.83(1)	1/4	1/8	0.875(1)	0.0038(4)
MgX2	16e	0.07(1)	1/4	1/8	0.875(1)	0.0038(4)
NaX2	16e	0.07(2)	1/4	1/8	0.875(1)	0.0038(4)
FeX2	16e	0.04(2)	1/4	1/8	0.875(1)	0.0038(4)
FeY	16c	0.455(15)	0	1/4	1/8	0.0038(4)
AlY	16c	0.27(1)	0	1/4	1/8	0.0051(5)
SiY	16c	0.17(2)	0	1/4	1/8	0.0051(5)
Ti+Cr	16c	0.07(4)	0	1/4	1/8	0.0051(5)
SiT1	8a		0	0	0	0.0063(3)
SiT2	16e		1/4	1/8	0.125(4)	0.0063(3)
O	32g		0.03(2)	0.80(2)	0.782(2)	0.006(2)
O	32g		0.66(5)	0.78(2)	0.18(1)	0.006(1)
O	32g		0.05(3)	0.407(3)	0.16(3)	0.006(1)
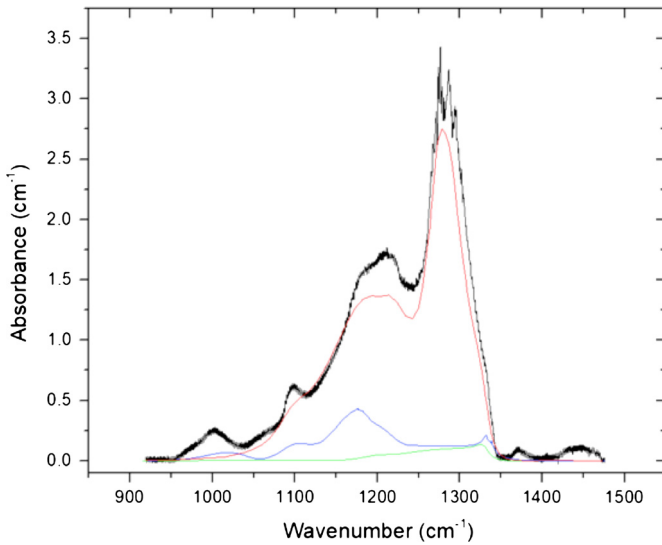
Fig. 3. Representative infrared transmission spectrum (black) of diamond ONZiZ-74 over the region of nitrogen-related defect bands. Red: Fitted spectrum of A-type defects, blue: B-type, green: D-type.

U = 0.040, V = 0.005, W = 0.007, and a Lorenzian mixing term of 0.38. The results are presented in Figs. 2b and c. Single crystal structure refinement converged to $R_F = 0.097$.

3.2. Diamond formation temperatures inferred from nitrogen defects using IR spectra

Infrared spectra of the diamond inclusion are shown in Fig. 3. Spectra were background subtracted. Contributions of A-, B-, and D-type defect bands were assessed by using the pure defect type spectra reported by Taylor et al. (1990). We used the calibrations by Boyd et al., (1994, 1995) for estimating the amount of nitrogen in A- and B-type defects and the calibration by Clark and Davey (1984) for D-type defects. The nitrogen abundance is assessed to 60–75 ppm and the percentage of A-defects of 78–84%. These values are consistent with formation and residence temperatures between 1400 and 1460K, rather independent on age: For instance a mantle residence time of 3 Ga would imply that the diamond grew at 1400 ± 10 K, whereas a residence time of 0.1 Ga corresponds to 1490 ± 10 K (Taylor et al., 1990).

3.3. Elemental abundances of the diamond inclusion

The bulk elemental abundances of the studied inclusion are given in Table 1, and are plotted in Figs. 4 and 5. The studied multiphase inclusion is silicate-undersaturated (Fig. 5a), with $Na_2O + K_2O$ up to 8.8 wt% (Table 1). The average elemental compositions of different OIB suites are correlated with their isotopic compositions (Jackson and Dasgupta, 2008; Huang et al., 2017; Figs. 4 and 5). This allows us to correlate the elemental features measured in the diamond inclusion with OIB endmembers normally characterized by their isotopic compositions. For example, CaO/Al_2O_3 and Th/Y are correlated with $^{206}Pb/^{204}Pb$ in global OIBs, with the newly found Bermuda HIMU lavas defining the high-$^{206}Pb/^{204}Pb$, $-CaO/Al_2O_3$ and $-Th/Y$ end. Our diamond inclusion has even higher CaO/Al_2O_3 and Th/Y than HIMU OIBs, and plots on the extension of the CaO/Al_2O_3 vs. Th/Y trend defined by global OIBs (Figs. 5b and 5c). In summary, this diamond inclusion either matches and/or plots at the extension of that of HIMU OIBs, such as Bermuda, St Helena, and Cook-Austral (Figs. 4 and 5), and it is markedly different from that of inclusions in lithospheric and ultra-deep source diamonds (Fig. 4b).
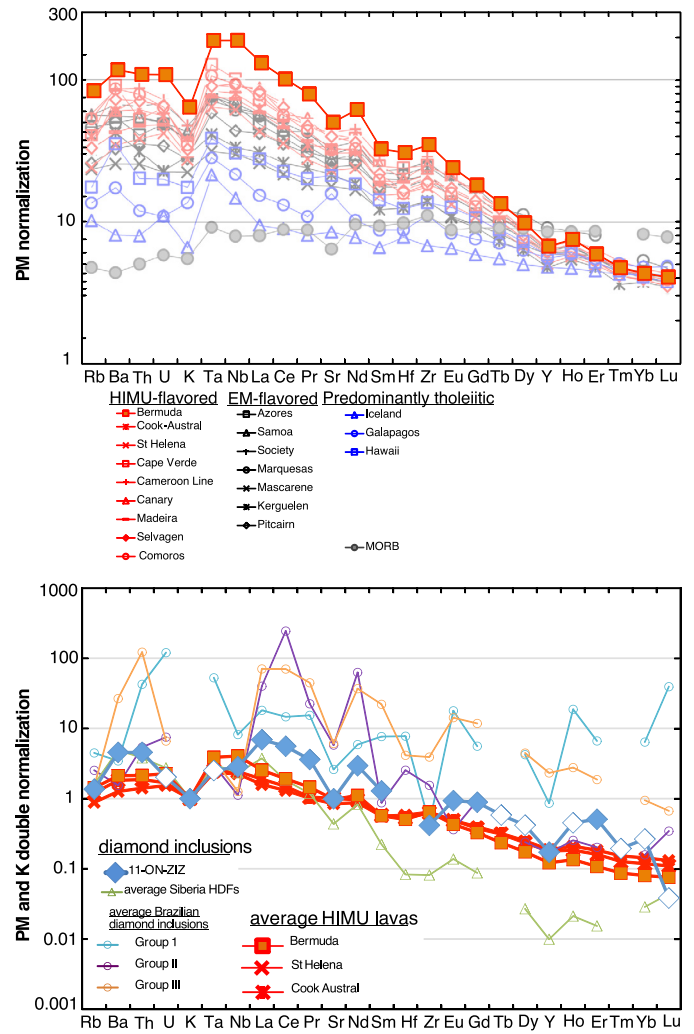

Fig. 4. a. Primitive mantle (PM) (McDonough and Sun, 1995) normalized multiple trace element patterns for average OIBs. OIB data are from the compilation of Huang et al. (2017), and Bermuda data are from Mazza et al. (2019). MORB averages are from Gale et al. (2013). Only OIBs with 8%<MgO<16% are included to minimize crystal fractionation effect. b. Primitive mantle (McDonough and Sun, 1995) and K double normalized multiple trace element patterns for the deep diamond inclusion (11-ON-ZIZ, this study) and the averages of HIMU lavas from Bermuda (Mazza et al., 2019), St Helena and Cook Austral (averages from summary in Huang et al. (2017)). Open symbols of 11-ON-ZIZ data show values that are higher than background, but not resolvable at 3 standard deviation level (Table 1). The averages of several diamond inclusions from other studies are also shown for comparison. Specifically, high-Mg carbonatitic high-density fluids (HDFs) in Siberian diamonds (Weiss et al., 2011) have a steeper trend. In contrast, Brazilian diamond inclusions (Timmerman et al., 2019), some of which have high $^3He/^4He$, have shallower trends.

In the chemical analysis, high Cu, Zn and Pb concentrations were found (Table 1). This is result of simultaneous ablation of the multiphase silicate-oxide inclusion and a sulfide inclusion, which is seen in the XRD map 6-8 μm away from the multiphase inclusion. Consequently, the Pb data could not be interpreted as part of the multiphase inclusion chemistry.

4. Discussions

4.1. Diamond inclusion entrapment pressure-temperature conditions

Pressure and temperature of diamond formation were obtained through two complementary methods shown in Fig. 6a: 1) Garnet geobarometry (Collerson et al., 2010; Wijbrans et al., 2014) (black rectangle), and 2) The isomeke pressure-temperature (P-T) path (P-T paths in strain-equilibrium of diamond host and inclusion)
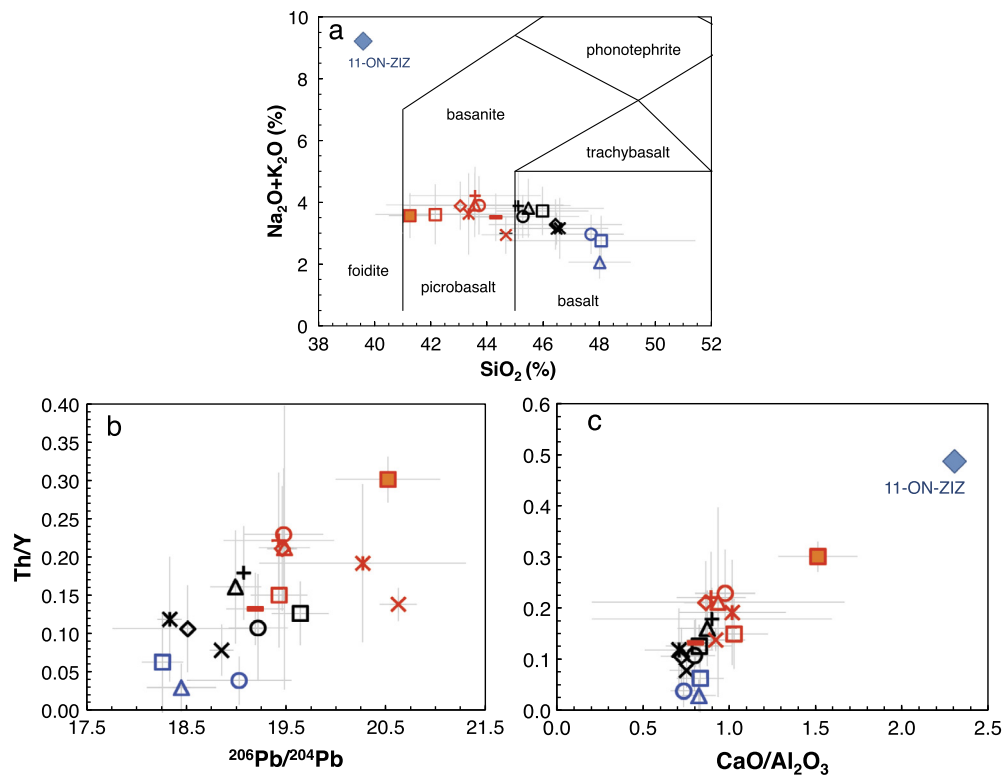
Fig. 5. SiO$_2$ vs. Na$_2$O + K$_2$O (**a**), Th/Y vs. ^{206}Pb/^{204}Pb (**b**) and CaO/Al$_2$O$_3$ (**c**) for OIB averages and the studied multiphase diamond inclusion. One standard deviations of OIB averages are plotted to show OIB variations. Our diamond inclusion plots on the extension of OIB trend. Legend: see Fig. 4. Data source: see Fig. 4 caption.

for ilmenite (grey area), which was calculated based on known thermoelastic parameters of this mineral (Tronche et al., 2010). Because of the compositional complexity of the garnet and sodic TAP, we only used ilmenite for combined isomeke P-T assessment following the approach used in Tschauner et al. (2018). The phase boundary between ilmenite and liuite was taken from Ming et al. (2006). We constrained the diamond formation P-T condition through the intersection of the ilmenite isomeke P-T path with the garnet barometric pressures (Fig. 6a). The intersection starts at 14 GPa, and 1250–1800 K (Fig. 6a).

As an independent check, we used the nitrogen-aggregation state in the host diamond to constrain formation temperature. As shown in Section 3.2, we estimated a nitrogen content of 60–75 ppm, and the percentage of A-defects of 78–84%. These values infer the formation and residence temperatures between 1400 and 1460 K, independent of the diamond age. As we show in Fig. 6, this range of temperature matches closely the intersection point of the ilmenite P-T path with the lower limit of the garnet barometric estimate.

All parameters taken together yield a pressure of 14.5 ± 0.5 GPa and a temperature of 1450 ± 50 K for the diamond inclusion entrapment. This is shown in Fig. 6. Entrapment in diamond indicates that the fluid also contained carbonate, which was reduced to diamond-forming carbon (Rohrbach and Schmidt, 2011; Thomson et al., 2016). The diamond inclusion entrapment conditions of 14.5 ± 0.5 GPa and 1450 ± 50 K plot right on top of the solidus of alkaline carbonated MORB (Fig. 6b; Litasov et al., 2013; Thomson et al., 2016), and match the formation of carbonatitic melt from subducted slabs plus diamond formation from reaction of carbonate with iron (Rohrbach and Schmidt, 2011).

4.2. HIMU geochemical signature from the transition zone

As shown in Figs. 4 and 5, our studied multiphase inclusion has a HIMU-type elemental pattern, and this geochemical signature is different from that of lithospheric and ultra-deep source diamond inclusions. The mineralogy of our inclusion, majorite-rich garnet, sodic TAP, ilmenite, and liebermannite, is consistent with formation around 14 GPa 1400-1500 K over an extensive range of alkaline rich bulk compositions (Litasov and Ohtani, 2005; Greaux et al., 2018). At these conditions the stable phase assembly is garnet + ilmenite + liebermannite + clinopyroxene + stishovite + fluid (Litasov and Ohtani, 2005). Upon ascent clinopyroxene, stishovite, and fluid reacted to form Na-bearing TAP. Thus, the presence of TAP shows that the HIMU source is water-saturated. Hence, through this inclusion we can correlate HIMU component with a specific depth and a particular regime of temperature and petrology in the mantle.

Overall, we have identified the endmember HIMU geochemical signature in a silicate inclusion entrapped in a diamond from the transition zone. It implies that the HIMU source is most likely a MORB-like material enriched in Ca and alkalis. This is fully consistent with previous geochemical assessments, which proposed the HIMU mantle source to be ancient recycled altered MORB (e.g., Chauvel et al., 1992; Mazza et al., 2019), probably with ancient marine carbonates (e.g., Castillo, 2015; Weiss et al., 2016), and is potentially located in the transition zone (Mazza et al., 2019). However, beyond these studies, we now show that the HIMU source region is located at the upper limit of the transition zone. Moreover, we conclude that HIMU endmember lavas form at temperatures of average to hot subducting slabs. OIBs form a continuous isotopic and compositional spectrum, which can be explained using a limited number of mantle endmembers (White et al., 2015; Figs. 4 and 5), and the HIMU endmember contributes variably to global OIBs. Our findings indicate that HIMU-dominated OIBs like Bermuda, St Helena, and Cook-Austral originate from the shallow transition zone, in conjunction with subduction of oceanic crust. Geophysical and geochemical findings indicate that some other OIBs originate from much greater depth than 420–440 km but still exhibit a contribution from the HIMU component, though less
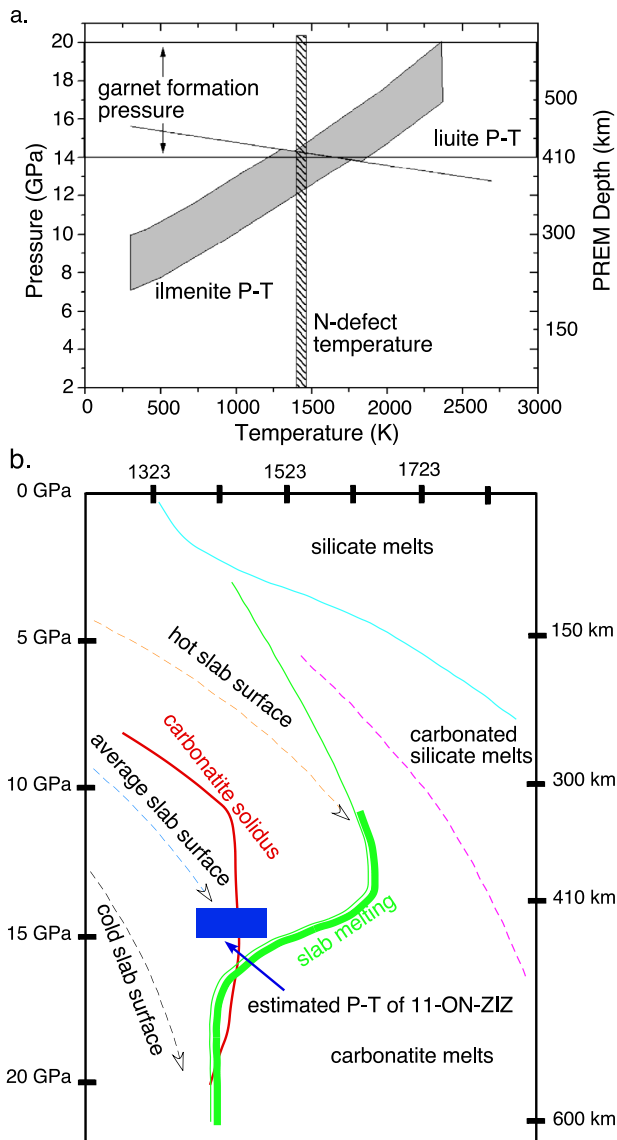
Fig. 6. Pressure-temperature assessment of the inclusion in diamond ONZiZ-74. The horizontal open box shows the garnet formation pressure. The grey area shows the ilmenite-liuite isomeke P-T path. The vertical hatched bar shows the N-defect temperature. See text for details. **b.** The estimated entrapment P-T condition of diamond inclusion 11-ON-ZIZ plotting on a phase diagram of carbonated MORB (Thomson et al., 2016). The red line shows the alkaline carbonatite solidus from Litasov et al. (2013). The different solidus P-T of Thomson et al. (2016) (green) and Litasov et al. (2013) (red) may be caused by different starting compositions in two studies. Our estimated entrapment P-T condition of 11-ON-ZIZ plots right on the carbonatite solidus of Litasov et al. (2013).

dominant than in Bermuda, St Helena, and Cook-Austral (White et al., 2015; Montelli et al., 2004; Humayun et al., 2004; Jackson and Dasgupta, 2008; Trela et al., 2017; Figs. 4 and 5). A plausible explanation is that upwellings of deep mantle plumes mobilize the HIMU-source in the shallow transition zone during ascent. This suggests that HIMU source is a global layer equivalent to the fluid- and incompatible element-rich layer at the upper boundary of the transition zone that has been proposed by Bercovici and Karato (2003). Our findings are consistent with this model.

5. Summary

We found that the geochemical signature of a multiphase inclusion in a diamond from the upper transition zone matches that of the HIMU OIBs. Pressure, temperature, and bulk composition of the inclusion indicate formation linked to subducted MORB at conditions of partial melting of wet carbonated MORB in the transition zone. HIMU-dominated mantle plumes (e.g., Bermuda, St. Helena, Cook-Austral islands), many of which are in the Atlantic Ocean, may originate predominantly from this region of the mantle. Subduction during the closing of the Atlantic Ocean may have loaded the transition zone beneath the Atlantic Ocean with HIMU source material. On the other hand, the ubiquitous presence of the HIMU geochemical signature in global OIBs is the result of entrainment of transition zone material by mantle plumes of deeper origin, and suggests HIMU to be a globally present layer or very common feature within the shallow transition zone.

Appendix A. Supplementary material

Supplementary material related to this article can be found online at https://doi.org/10.1016/j.epsl.2020.116323.

References

Angel, R.J., Mazzucchelli, M.L., Alvaro, M., Nimis, P., Nestola, F., 2014. Geobarometry from host-inclusion systems: the role of elastic relaxation. Am. Mineral. 99, 2146–2149.

Ballaran, T.B., Liu, J., Dubrovinsky, L.S., Caracas, R., Crichton, W., 2009. High-pressure ferroelastic phase transition in aluminosilicate hollandite. Phys. Rev. B 80, 214104.

Bercovici, D., Karato, S., 2003. Whole-mantle convection and the transition-zone water filter. Nature 425, 39–44.

Boyd, S.R., Kiflawi, I., Woods, G.S., 1994. The relationship between infrared absorption and the A defect concentration in diamond. Philos. Mag. B 69, 1149–1153.

Boyd, S.R., Kiflawi, I., Woods, G.S., 1995. Infrared absorption by the B nitrogen aggregate in diamond. Philos. Mag. B 72, 351–361.

Brandon, A.D., Walker, R.J., 2005. The debate over core-mantle interaction. Earth Planet. Sci. Lett. 232, 211–225.

Castillo, P.R., 2015. The recycling of marine carbonates and sources of HIMU and FOZO ocean island basalts. Lithos 216–217, 254–263.

Chauvel, C., Hofmann, A.W., Vidal, P., 1992. HIMU-EM: the French Polynesian connection. Earth Planet. Sci. Lett. 110, 99–119.

Chauvel, C., Maury, R.C., Blais, S., Lewin, E., Guillou, H., Guille, G., Rossi, P., Gutscher, M.A., 2012. The size of plume heterogeneities constrained by Marquesas isotopic stripes. Geochem. Geophys. Geosyst. 13, Q07005.

Clark, C.D., Davey, S.T., 1984. One-phonon infrared absorption in diamond. J. Phys. C 17, 1127–1140.

Collerson, K.D., Williams, Q., Kamber, B.S., Omori, S., Arai, H., Ohtani, E., 2010. Majoritic garnet: a new approach to pressure estimation of shock events in meteorites and the encapsulation of sub-lithospheric inclusions in diamond. Geochim. Cosmochim. Acta 70, 5939–5957.

Dera, P., Zhuravlev, K., Prakapenka, V., Rivers, M.L., Finkelstein, G.J., Lavina, B., Grubor-Urosevic, O., Tschauner, O., Clark, S.M., Downs, R.T., 2013. High pressure single-crystal micro X-ray diffraction analysis with GSE_ADA/RSV software. High Press. Res. 34, 1–19.

Gale, A., Dalton, C.A., Langmuir, C.H., Su, Y., Schilling, J.G., 2013. The mean composition of ocean ridge basalts. Geochem. Geophys. Geosyst. 14, 489–518.

Grassi, D., Schmidt, W.M., Günther, D., 2012. Element partitioning during carbonated pelite melting at 8, 13, and 22 GPa and the sediment signature in the EM mantle components. Earth Planet. Sci. Lett. 327–328, 84–96.

Greaux, S., Nishi, M., Tateno, S., Kuwayama, Y., Hirao, N., Kawai, K., Maruyama, S., Irifune, T., 2018. High-pressure phase relation of KREEP basalts: a clue for finding the lost Hadean crust? Phys. Earth Planet. Inter. 274, 184–194.

Hart, S.R., 1984. A large-scale isotope anomaly in the Southern Hemisphere mantle. Nature 309, 753–757.

Hazen, R.M., Downs, R.T., Finger, L.W., Conrad, P.G., Gasparik, T., 1994. Crystal chemistry of Ca-bearing majorite. Am. Mineral. 79, 581–584.

Howe, H., Pawley, A.R., 2019. The effect of solid solution on the stability of talc and 10-Å phase. Contrib. Mineral. Petrol. 174, 81.

Huang, S., Hall, P.S., Jackson, M.G., 2011. Geochemical zoning of volcanic chains associated with Pacific hotspots. Nat. Geosci. 4, 874–878.

Huang, S., Zheng, Y.F., 2017. Mantle geochemistry: insights from ocean island basalts. Sci. China Earth Sci. 60, 1976–2000.

Humayun, M., Qin, L., Norman, M.D., 2004. Geochemical evidence for excess iron in the mantle beneath Hawaii. Science 306, 91–94.

Jochum, K.P., Willbold, M., Raczek, I., Stoll, B., Herwig, K., 2005. Chemical characterization of the USGS reference glasses GSA-1G, GSC-1G, GSD-1D, GSE-1G, BCR-2G, BHVO-2G and BIR-1G using EPMA, ID-TIMS, ID-ICP-MS and LA-ICP-MS. Geostand. Geoanal. Res. 29, 285–302.

Jackson, M.G., Dasgupta, R., 2008. Compositions of HIMU, EM1, and EM2 from global trends between radiogenic isotopes and major elements in ocean island basalts. Earth Planet. Sci. Lett. 276, 175–186.

Kraus, W., Nolze, G., 1996. PowderCell – a program for the representation and manipulation of crystal structures and calculation of the resulting X-ray powder patterns. J. Appl. Crystallogr. 29 (3), 301–303.

Litasov, K.D., Ohtani, E., 2005. Phase relations in hydrous MORB at 18-28 GPa: implications for heterogeneity of the lower mantle. Phys. Earth Planet. Inter. 150, 239–263.

Litasov, K.D., Shatskiy, A., Ohtani, E., Yaxley, G.M., 2013. Solidus of alkaline carbonatite in the deep mantle. Geology 41, 79–82.

Ma, C., Tschauner, O., Beckett, J.R., Rossman, G.R., Prescher, C., Prakapenka, V.B., Bechtel, H.A., MacDowell, A., 2018. Liebermannite, $KAlSi_3O_8$, a new shock-metamorphic, high-pressure mineral from the Zagami Martian meteorite. Meteorit. Planet. Sci. 53, 50–61.

Ma, C., Tschauner, O., Beckett, J.R., Liu, Y., Greenberg, E., Prakapenka, V.B., 2019. Chenmingite, $FeCr_2O_4$ in the $CaFe_2O_4$-type structure, a shock-induced, high-pressure mineral in the Tissint martian meteorite. Am. Mineral. 104, 1521–1525.

Mazza, S.E., Gazel, E., Bizimis, M., Moucha, R., Beguelin, P., Johnson, E.A., McAleer, R.J., Sobolev, A.V., 2019. Sampling the volatile-rich transition zone beneath Bermuda. Nature 569, 398–403.

McDonough, W.F., Sun, S.-s., 1995. The composition of the Earth. Chem. Geol. 120, 223–253.

Ming, L.C., Kim, Y.-H., Uchida, T., Wang, Y., Rivers, M., 2006. In situ X-ray diffraction study of phase transitions of $FeTiO_3$ at high pressures and temperatures using a large-volume press and synchrotron radiation. Am. Mineral. 91, 120–126.

Montelli, R., Nolet, G., Dahlen, F.A., Masters, G., Engdahl, E.R., Hung, S.-H., 2004. Finite-frequency tomography reveals a variety of plumes in the mantle. Science 303, 338–343.

Prescher, C., Prakapenka, V.B., 2015. DIOPTAS: a program for reduction of two-dimensional X-ray diffraction data and data exploration. High Press. Res. 35 (3), 223–230.

Putz, H., Schön, J.C., Jansen, M., 1999. Combined method for ab initio structure solution from powder diffraction data. J. Appl. Crystallogr. 32, 864–870.

Ringwood, A.E., Reid, A.F., Wadsley, A.D., 1967. High-pressure $KAlSi_3O_8$, an aluminosilicate with sixfold coordination. Acta Crystallogr. 23, 1093–1095.

Rizo, H., Andrault, D., Bennett, N.R., Humayun, M., Brandon, A., Vlastelic, I., Moine, B., Poirier, A., Bouhifd, M.A., Murphy, D.T., 2019. ^{182}W evidence for core-mantle interaction in the source of mantle plumes. Geochem. Perspect. Lett. II, 6–11.

Rohrbach, A., Schmidt, M.W., 2011. Redox freezing and melting in the Earth's deep mantle resulting from carbon-iron redox coupling. Nature 472, 209–212.

Taylor, W.R., Jaques, A.L., Ridd, M., 1990. Nitrogen-defect aggregation characteristics of some Australasian diamonds: time-temperature constraints on the source regions of pipe and alluvial diamonds. Am. Mineral. 75, 1290–1310.

Thomson, A.R., Walter, M.J., Kohn, S.C., Brooker, R.A., 2016. Slab melting as a barrier to deep carbon subduction. Nature 529, 76–79.

Timmerman, S., Honda, M., Burnham, A.D., Amelin, Y., Woodland, A., Pearson, D.G., Jaques, A.L., Le Losq, C., Bennett, V.C., Bulanova, G.P., Smith, C.B., Harris, J.W., Tohver, E., 2019. Primordial and recycled helium isotope signatures in the mantle transition zone. Science 365, 692–694.

Trela, J., Gazel, E., Sobolev, A.V., Moore, L., Bizimis, M., Jicha, B., Batanova, V.G., 2017. The hottest lavas of the Phanerozoic and the survival of deep Archaean reservoirs. Nat. Geosci. 10, 451–455.

Tronche, E.J., van Kan Parker, M., de Vries, J., Wang, Y., Sanehira, T., Li, J., Chen, B., Gao, L., Klemme, S., McCammon, C.A., van Westrenen, W., 2010. The thermal equation of state of $FeTiO_3$ ilmenite based on in situ X-ray diffraction at high pressures and temperatures. Am. Mineral. 95, 1708–1716.

Tschauner, O., Huang, S., Greenberg, E., Prakapenka, V., Ma, C., Rossman, G., Shen, A.H., Zhang, D., Newville, M., Lanzirotti, A., Tait, K., 2018. Ice-VII inclusions in diamonds: evidence for aqueous fluid in Earth's deep mantle. Science 359, 1136–1139.

Wang, X.-J., Chen, L.-H., Hofmann, A.W., Mao, F.-G., Liu, J.-Q., Zhong, Y., Xie, L.-W., Yang, Y.-H., 2017. Mantle transition zone-derived EM1 component beneath NE China: geochemical evidence from Cenozoic potassic basalts. Earth Planet. Sci. Lett. 465, 16–28.

Wechsler, B.A., Prewitt, C.T., 1984. Crystal structure of ilmenite ($FeTiO_3$) at high temperature and at high pressure. Am. Mineral. 69, 176–185.

Weis, D., Garcia, M.O., Rhodes, J.M., Jellinek, M., Scoates, J.S., 2011. Role of the deep mantle in generating the compositional asymmetry of the Hawaiian mantle plume. Nat. Geosci. 4, 831–838.

Weiss, Y., Griffin, W.L., Bell, D.R., Navon, O., 2011. High-Mg carbonatitic melts in diamonds, kimberlites and the sub-continental lithosphere. Earth Planet. Sci. Lett. 309, 337–347.

Weiss, Y., Class, C., Goldstein, S.L., Hanyu, T., 2016. Key new pieces of the HIMU puzzle from olivines and diamond inclusion. Nature 537, 666–670.

White, W.M., 2015. Isotopes, DUPAL, LLSVPs, and anekantavada. Chem. Geol. 419, 10–28.

Wijbrans, C.J., Niehaus, O., Rohrbach, A., Pöttgen, R., Klemme, S., 2014. Thermodynamic and magnetic properties of knorringite garnet ($Mg_3Cr_2Si_3O_{12}$) based on low-temperature calorimetry and magnetic susceptibility measurements. Phys. Chem. Miner. 41, 341–346.

Williams, C.D., Mukhopadhyay, S., Rudolph, M.L., Romanowicz, B., 2019. Primitive helium is sourced from seismically slow regions in the lowermost mantle. Geochem. Geophys. Geosyst. 20, 4130–4145.

Yamanaka, T., Komatsu, Y., Nomori, H., 2007. Electron density distribution of $FeTiO_3$ ilmenite under high pressure analyzed by MEM using single crystal diffraction intensities. Phys. Chem. Miner. 34, 307–318.

Yang, S., Humayun, M., Righter, K., Jefferson, G., Fields, D., Irving, A.J., 2015. Siderophile and chalcophile element abundances in shergottites: Implications for Martian core formation. Meteorit. Planet. Sci. 50, 691–714.